Integration of quantum dot light sources

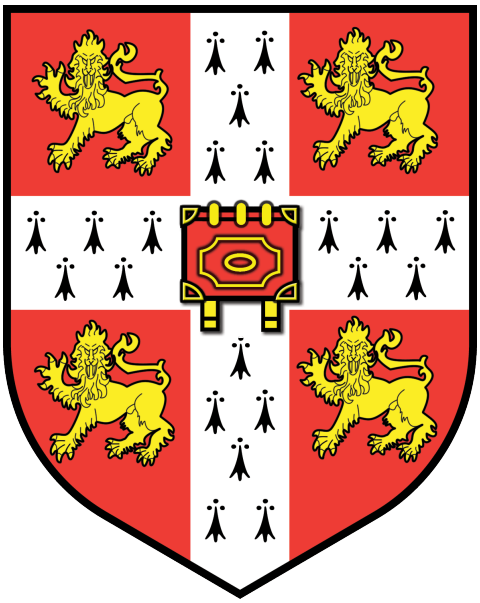

Eoin Murray

Magdalene College

Department of Physics

University of Cambridge

2015

This dissertation is submitted for the degree of

Master of Philosophy

Declaration

This dissertation is the result of my own work and includes nothing which is the outcome of work done in collaboration, except as stated in the Acknowledgements and specified in the text.

It is not substantially the same as any that I have submitted, or, is being concurrently submitted for a degree or diploma or other qualification at the University of Cambridge or at any other University or similar institution.

No substantial part of my dissertation has already been submitted, or, is being concurrently submitted for a degree or diploma or other qualification at the University of Cambridge or at any other University or similar institution.

Acknowledgements

This project was very much a team effort and I would first like to thank all the members of the integration project team. Thanks to David Ellis for designing and fabricating the devices, the devices were fabricated at the Cavendish and the e-beam lithography was undertaken by Jonathan Griffiths. Thanks to Thomas Meany for packaging the hybrid device and taking measurements, Frederick Floether for designing the devices, Jamie Lee for assisting with measurements and to Anthony Bennet for designing and taking measurements. Thanks also for Ian Farrer and the staff at the Cavendish for growing wafers. Thanks to Andrew Shields and David Ritchie for giving me this opportunity to study for this degree. This project was supported by the Initial Training Network PICQUE under the European Commission Marie Curie Actions.

Abstract

Fundamental to the future of quantum photonics is the ability to create integrated devices. An integrated chip offers intrinsic stability and compactness. This makes it inherently more scalable than a bulk optics approach. Quantum dots (QDs) are a developing on-chip source of single photons. This project aims to take quantum dots embedded in a III-V material and combine them with integrated waveguide components. The InAs QDs are grown in GaAs substrate and are bonded to a SiON based waveguide platform. This approach has potential for the realization of an efficient coupling between the quantum dots and the waveguides and then on-chip manipulation of the emitted photons. In this report, the results thus far will be presented and proposals for future designs will be discussed.

Publications resulting from this work

Quantum photonics hybrid integration platform

E. Murray, D. J. P. Ellis, T. Meany, F. F. Floether, J. P. Lee, J. P. Griffiths, G. A. C. Jones, I. Farrer, D. A. Ritchie, A. J. Bennett, and A. J. Shields.

Applied Physics Letters 107.17 (2015): 171108.

Editor's choice 2-8th November 2015

Cavity-enhanced coherent light scattering from a quantum dot A. J. Bennett, J. P. Lee, D. J. P. Ellis, T. Meany, **E. Murray**, F. F. Floether, J. P. Griffiths, I. Farrer, D. A. Ritchie, and A. J. Shields.

arXiv pre-print: 1508.01637v1

An all-electric scalable and tuneable single-photon source E. Murray & J. P. Lee, A. J. Bennett, J. Skiba-Szymanska, D. J. P. Ellis, I. Farrer, D. A. Ritchie, and A. J. Shields.

In-preparation

Conferences

Quantum dots for quantum information science,

E. Murray

PICQUE Integrated Quantum Photonics Workshop, 7-9 January 2015, Oxford, UK

Quantum photonics hybrid integration platform

E. Murray, D. J. P. Ellis, T. Meany, F. F. Floether, J. P. Lee, J. P. Griffiths, G. A. C. Jones, I. Farrer, D. A. Ritchie, A. J. Bennett, and A. J. Shields.

Best talk awarded PICQUE Roma Scientific School, 6-10 July 2015, Rome, Italy

Contents

1 Introduction and theory. 6

1.1 Introduction to Quantum dots 6

1.1.1 Single photon emission from Quantum dots 8

1.2 Semiconductor waveguides 9

1.2.1 Two dimensional waveguides 12

1.2.2 Directional couplers and Mach Zehnder interferometers 13

1.3 Integrated quantum devices 14

1.3.1 NOON states and quantum sensing 15

1.4 Conclusion 18

2 Methods and fabrication. 19

2.1 Waveguide fabrication and characterisation 19

2.1.1 Directional coupler ratio measurement 20

2.1.2 Mach Zehnder interferometer visibility measurement 22

2.2 Quantum dot growth and characterisation 22

2.2.1 Molecular beam epitaxy growth 22

2.2.2 Optical characterisation of quantum dots. 24

2.2.3 Hanbury-Brown and Twiss measurements 25

2.3 Hybrid device 26

2.3.1 Characterisation of quantum dots in hybrid circuit. 27

3 Results **28**

3.1 Simulations and design 29

3.2 Waveguide devices 30

3.3 Hybrid integrated devices 33

4 Future work **39**

Chapter 1

Introduction and theory.

Linear optical quantum computing (LOQC) has been proven to be computationally efficient with a single photon source and a series of beamsplitters and phase shifters [1]. Some implementations of two photon gates have been realised with bulk optics [2], however a scalable LOQC is unfeasible with bulk optics and an integrated technology is needed [3]. Semiconductor waveguides with integrated quantum dots (QD) are a promising solution. Semiconductor III-V QDs have been shown to have good, bright, single photon emission [4], can emit indistinguishable and entangled photons [5, 6], can be site-controlled [7] and are compatible with semiconductor foundry techniques. Progress is being made to embed the QDs into integrated waveguide platforms. Integrated photonics offers the potential for true scalability due to component miniaturisation. Stability is intrinsic to the platform and offers a reduction in complexity and size of the device [8]. Many of the elements needed for LOQC can be manufactured on-chip, high fidelity beam splitters and Mach Zehnder interferometers (MZIs) can be made in various semiconductors [9, 10, 11] as well as on-chip detectors [12, 13] however further work is needed to integrate these components on with a quantum light source.

1.1 Introduction to Quantum dots

Semiconductor quantum dots (QDs) are islands of a certain material surrounded by a material of a higher band gap. The QD region is a three dimensional structure which confines carriers in

all dimensions, giving carries freedom to move in zero dimensions. This confinement gives rise to discrete energy levels inside the QD.

Normally a QD will confine two electron levels and two hole levels, more may be accommodated in a larger QD. Each level will only confine two carriers due to the Pauli exclusion principle. Figure 1.1 shows the electronic structure of a QD. An electron excited to the conduction band leave a hole in the valence band and is referred to as an e-h pair. An e-h pair confined in the QD is referred to as an exciton, two e-h pairs is a biexciton. When there is an imbalance in the number of electrons and holes a charged exciton is created. Electron-hole pairs can be excited into the quantum dot by numerous methods - primarily electro and photo-excitation. In the non-resonant case, carriers are created in the vicinity of the QD by an above band excitation laser or an electric current. These carriers will relax into the available quantum potentials, the lowest energy of which is typically the QD.

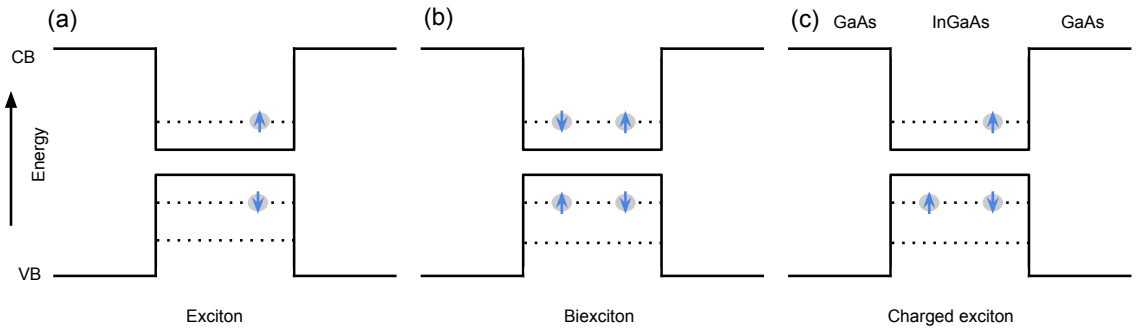

Figure 1.1: Electronic structure of a quantum dot. (a) An e-h pair is referred to as an exciton. (b) Two e-h pairs is referred to as a biexciton. (c) An exciton with an extra hole (electron) is a positively (negatively) charged exciton.

The discrete energy levels in the QD give rise to clean, sharp emission lines. There is a well defined energy for each transition and as such the emitted photons have a well defined wavelength, limited by the lifetime of the state.

1.1.1 Single photon emission from Quantum dots

The angular momentum of an electron is $\pm 1/2$ and for a hole is $\pm 3/2$. The e-h pair can combine to make a state with spin ± 1 for photon emission and ± 2 for non-radiative recombination. The energy of the emitted photon corresponds to the energy of its original excitonic state. Thus the emitted photons can be spectrally filtered to analyse the emission from only one excitonic state.

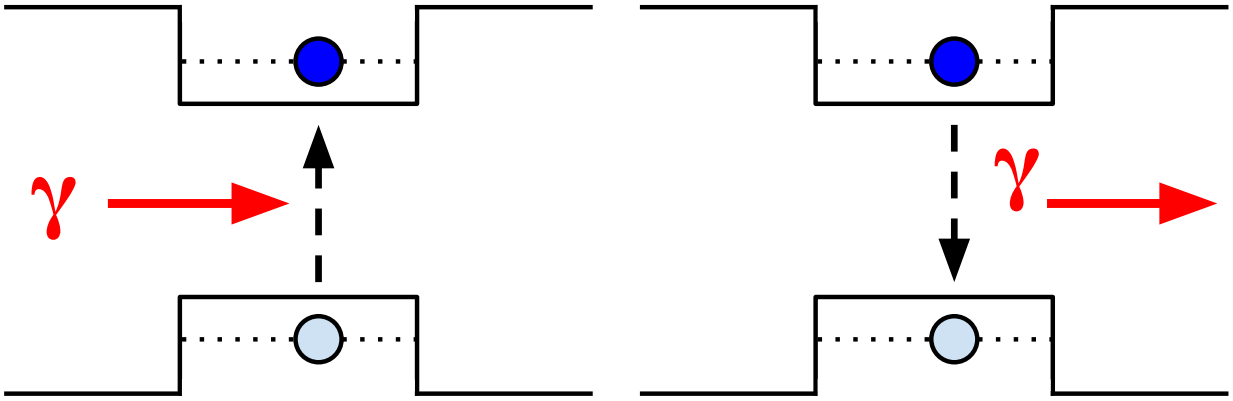

Figure 1.2: A single photon emission process in a quantum dot. A photon (γ in the image) excites an electron from the Valence band to the Conduction band, this creates an exciton. This exciton can relax into the quantum dot and after some time τ it will recombine and emit another photon. Since the quantum dot energy leves are discrete, and only accept a fixed number of carriers and after photon emission there is a finite time which must pass before more carriers can be captured, true single photon emission is possible.

For a light source with Poissonian emission statistics such as a laser, true single photon emission can not be achieved even with significant attenuation because the probability for multi photon emission still exists. In the case of a quantum dot, since each excitonic energy level can only accept a fixed number of carriers and after photon emission there is a finite time which must pass before more carriers can be captured, true single photon emission is possible. [**?**] This process is shown schematically in Figure 1.2. This single photon emission can be verified by measuring the two photon second order correlation function

$$g^{(2)}(\tau) = \frac{\langle I(t)I(t+\tau)\rangle}{\langle I(t)\rangle \langle I(t+\tau)\rangle} \tag{1.1}$$

This is achieved by doing a Hanbury Brown Twiss measurement [14]. A stream of single photons

impinge on a 50:50 beamsplitter. The two outputs of the beamsplitters are sent to single photon detectors. One of the detector signals is delayed by a time τ in order to measure both positive and negative correlation times. If the source is a true single photon source there will be a lack of coincidence clicks on both detectors when $\tau = 0$, and thus $g^{(2)}(0)$ will be zero. Single photon emission from QDs has been demonstrated under a wide range of excitation conditions: electrical (DC and AC) and optical (continuous wave (cw) and pulsed lasers at above band, quasi-resonant and resonant regimes).

1.2 Semiconductor waveguides

A dielectric waveguide consists of a core material surrounded by a second material of lower refractive index. The surrounding material is known as the waveguide cladding. Here the theory is set out as in Integrated Photonics by Saleh and Teich [15]. As an introduction to the design of waveguides in this section the prorogation of light in a symmetric dielectric slab waveguide will be discussed. A core slab of refractive index n_1 is clad by two slabs of refractive index n_2. This structure is shown in Figure 1.3. The critical angle for the total internal reflection of light is derived from Snells law to be

$$\theta_c = \arcsin \frac{n_1}{n_2}. \tag{1.2}$$

When light impinges on the boundary of n_1 and n_2 with an angle less than θ_c then it is reflected. Figure 1.3 shows a guided and an unguided ray of light. The unguided ray hits the boundary with an angle greater than θ_c and therefore some of the light refracts, losing some of the light at each reflection causing the ray to eventually vanish. The guided ray hits the boundary at an angle less than θ_c and reflects without any loss of power and will propagate along the core.

To understand the waveguide modes in the structure assume there is a transverse electromagnetic (TEM) plane wave propagating in the waveguide core. This TEM wave has a wavelength $\lambda = \lambda_0/n_1$ where λ_0 is the free space wavelength. The wave is reflected each time at the boundary with an angle less than θ_c so the wave propagates in the core without loss of power. With each reflection the

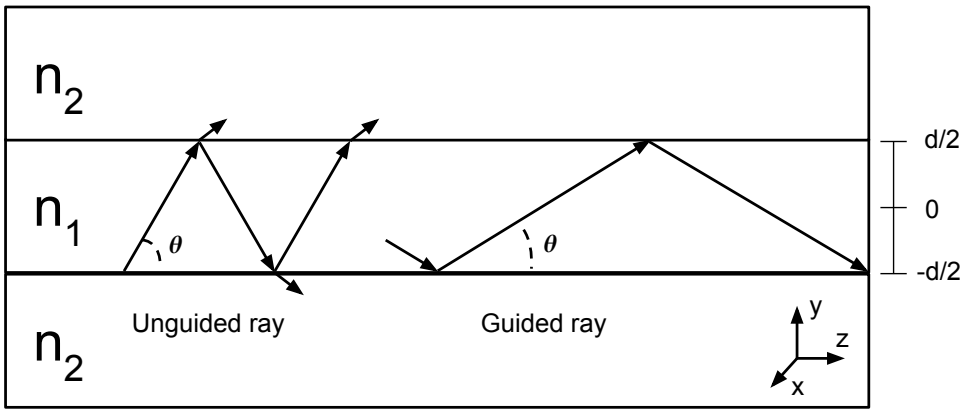

Figure 1.3: Light ray propagation in a planar dielectric waveguide. The unguided ray impinges on the boundary at angle larger than θ_c and therefore some of the light refracts, losing power at each reflection causing the ray to gradually disappear. The guided ray impinges at an angle less than θ_c and reflects fully propagating long the core without any loss of power.

wave lags behind the original by a distance $2d\sin\theta$ [15]. There is also a phase ϕ_r change induced by each internal reflection. There is now a self-consistency condition imposed upon the reflected wave. As the wave reflects twice it reproduces itself, waves which satisfy this condition are known as eigenmodes, or modes of the waveguide. The wave interferes with itself and a pattern is created which does not change with $\hat{z}$. Due to this self-consistency the phase shift between the waves is zero or a multiple of 2π, giving rise to the condition

$$2k_y d - 2\phi_r = 2\pi m, \qquad m = 0, 1, 2, ... \tag{1.3}$$

where $k_y = n_1 k_0 \sin\theta$. The phase shift ϕ_r in the transverse electric (TE) case due to total internal reflection is given by

$$\tan\frac{\phi_r}{2} = \sqrt{\frac{\sin^2\theta_c}{\sin^2\theta} - 1}. \tag{1.4}$$

Combining this with Equation 1.3 it is deduced that

$$\tan\left(\pi\frac{d}{\lambda}\sin\theta - m\frac{\pi}{2}\right) = \sqrt{\frac{\sin^2\theta_c}{\sin^2\theta} - 1} \tag{1.5}$$

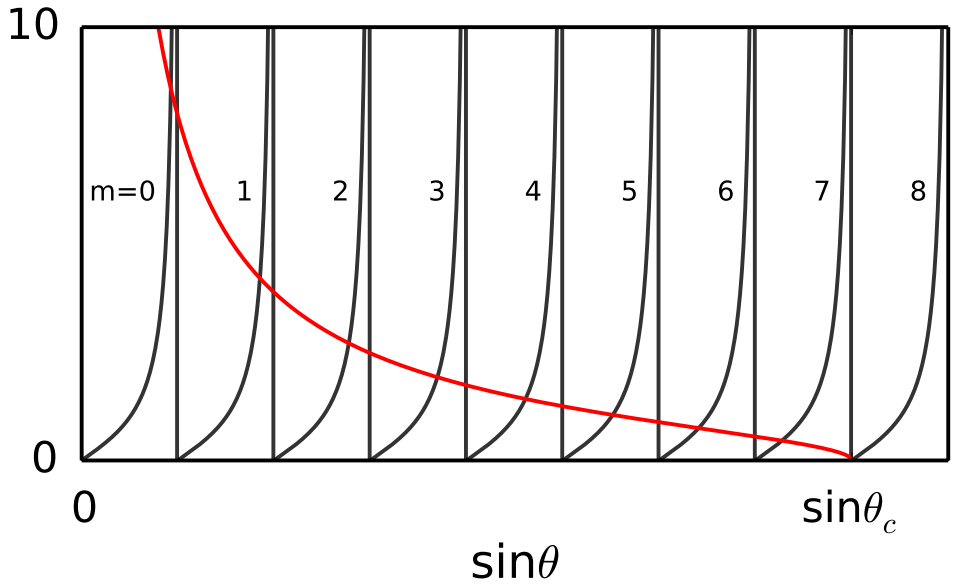

Figure 1.4: Graphical solution of to the transcendental equation 1.5. The black line is the LHS of the equation and the red line is the RHS. Each LHS segment corresponds to a mode in the waveguide.

This equation is transcendental and can be solved graphically, this solution is shown in Figure 1.4. The LHS is a set of tan, when m is even, and cot functions, when m is odd. Each LHS segment corresponds to a mode in the waveguide. When the LHS crosses the x-axis, indicated by the semicircles, $\sin\theta_m$ can be determined. The distance between these intersections is $\lambda/2d$. The solution for transverse magnetic (TM) is very similar, with just a different phase change upon reflection ϕ_r. This information can be used to deduce how many TE modes are in a waveguide of a given size d. The number of modes M is given by the amount of segments of width $\lambda/2d$ exist before $\sin\theta$ reaches the value $\sin\theta_c$.

$$M = \frac{\sin\theta_c}{\lambda/2d}, \tag{1.6}$$

rounded up to the nearest integer. By substituting $\cos\theta_c = n_2/n_1$ into Equation 1.2 it is seen that

$$M = 2\frac{d}{\lambda}\mathrm{NA} \tag{1.7}$$

where

$$\mathrm{NA} = \sqrt{n_1^2 - n_2^2} \tag{1.8}$$

is the numerical aperture (NA) of the waveguide. The NA defines the range of angle from which the waveguide can collect light. Equation is extremely important in waveguide design because it defines the single-mode cutoff for when $M \leq 1$. This impacts the choice of d and the wavelength for which the waveguide is single mode or multimode. Single mode waveguides are generally more useful for quantum optics because they allow two photon interference between light coming in from two single mode channels, this allows the operation of directional couplers and Mach Zehnder interferometers. Single mode optical fibres have lower loss in the telecommunications wavelength ranges and so is better suited to long distance communication.

1.2.1 Two dimensional waveguides

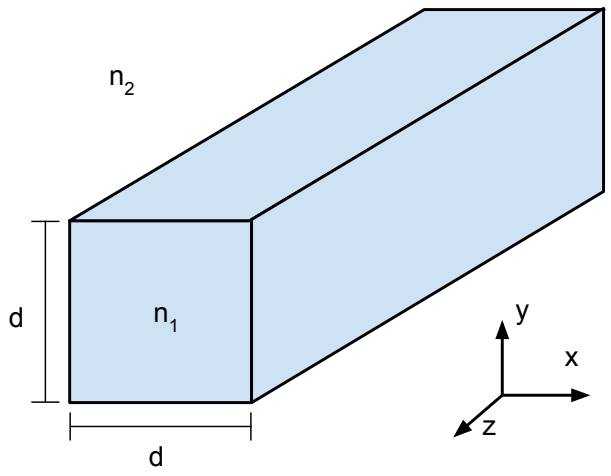

Figure 1.5: Index structure of a waveguide which confines light in two dimensions. The light is confined in $\hat{x}$ and $\hat{y}$ but is free to propagate in the $\hat{z}$ direction.

A two dimensional dielectric waveguide is one which confines light along two axes and allows the light to propagate freely along the third axis. A schematic of a rectangular waveguide is shown in Figure 1.5. The modes and number of modes can be derived in a similar fashion as for the planar dielectric waveguide and shall just be quoted here [15]. The number of modes in a two dimensional waveguide can be approximated by

$$M \approx \frac{\pi}{4}\left(\frac{2d}{\lambda_o}\right)^2 \mathrm{NA}^2. \tag{1.9}$$

This approximation holds well for multimode waveguides, but loses accuracy near the single mode boundary. Design of single mode two dimensional waveguides generally needs to be solved computationally.

1.2.2 Directional couplers and Mach Zehnder interferometers

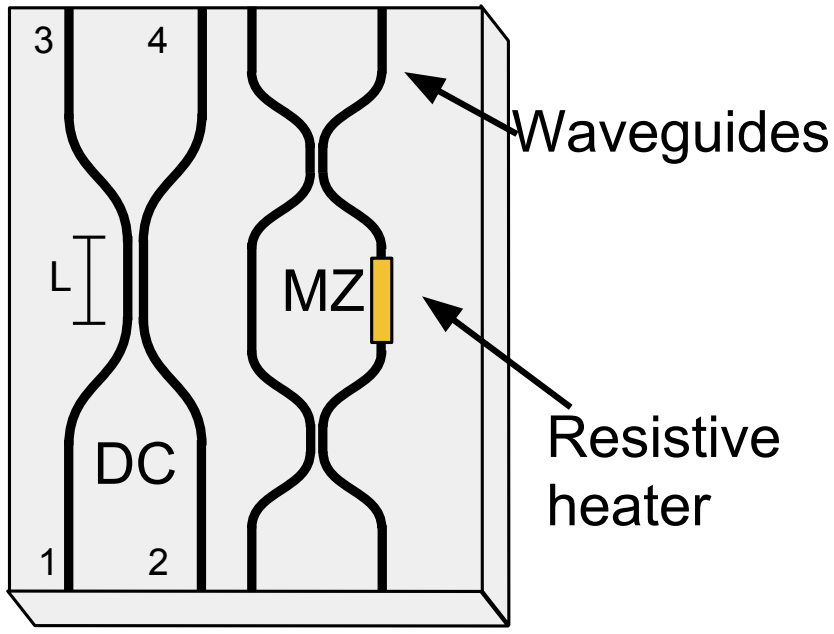

Figure 1.6: Two common waveguide devices, a directional coupler and a Mach Zehnder interferometer. The numbers on the directional couplers indicate input and output ports which shall be reference in the text, equivalent ports shall be used for the Mach Zehnder interferometer.

Figure 1.6 shows the schematic of two waveguide devices used frequently throughout this project. A directional coupler (DC) is a photonic device which splits the power between two output ports with a well defined coupling ratio between the ports. Two waveguides are brought close enough so that the evanescent fields overlap. The waveguides are assumed to be single mode. It can be derived that the power in each port 3 and 4 in Figure 1.6 as a result of light of power P_1 being injected to the coupler from port 1 is

$$P_3(z) = P_1 \cos^2 cz \tag{1.10}$$

$$P_4(z) = P_1 \sin^2 cz \tag{1.11}$$

Where z is the propagation direction and c is the coupling coefficient related to the index contrast of the waveguide, the separation d between the waveguides in the interaction region and the operating wavelength.

A Mach Zehnder interferometer (MZI) is a sequence of two DCs in series. The light splits 50/50 into two arms by the first DC. On one of the arms is a local refractive index changing element, this can be a electrode to take advantage of the electro-optic effect or heater, for the thermo-optic effect. Here it shall be assumed to be a heater. This element changes the local refractive index in the arms. This causes a phase mismatch between the light propagating in each arm so that the light will constructively or destructively interfere at the second DC. By tuning the heater this phase can be chosen an light can be arbitrarily coupled between ports 3 and 4. This is called a Mach Zehnder interferometer switch or modulator. These are used extensively in telecommunications to route signals between different channels.

1.3 Integrated quantum devices

Semiconductor quantum dots and waveguides are interesting technologies on their own. However this thesis focuses on the combination of these technologies to create a platform capable of making working integrated quantum devices in the future.

In Chapter 2 and 3, we attach a QD filled GaAs chip to the end of a silicon oxynitride (hereafter SiON) based photonic circuit. This approach allows us to make custom designed photonic circuits, which are fabricated separately from the QD quantum light source. The circuits are made up of a series of MZI's. This thesis focuses on the initial fabrication and demonstration of the platform. In the next phase of research there are many target circuits which are interesting for quantum telecommunications which have been demonstrated with QD's with bulk optics, but not yet reproduced on an integrated device. Theses include CNOT (controlled NOT) gates[16], quantum relays' [17], quantum amplifiers [18, 19], NOON state generation [20, 21, 22] and various combiners and splitters.

1.3.1 NOON states and quantum sensing

This section will describe a useful application of quantum sources and quantum circuits: generating a NOON state. The dynamics of a NOON state as it passes through a MZI allow it to be super sensitive to phase changes in the MZI [21, 23]. A NOON state is a many particle quantum entangled state represented as:

$$|\psi\rangle = |N\rangle_a |0\rangle_b + e^{iN\theta} |0\rangle_a |N\rangle_b \tag{1.12}$$

this state is a superposition of N particles in mode a and 0 particles in mode b and vica-versa. The particles need to be bosonic and in this case the quantum particles are photons.

To generate this state using photonics we consider the state generated by photons propagating through an MZI. In the single photon case, single-photon interference occurs from the path length difference in the two arms of the MZI. One of the photon modes gathers a phase shift $\Delta\phi$ and causes the detection probabilities of the MZI output arms to change.

The probabilities become $P_1 = 1 + \cos\Delta\phi$ and $P_2 = 1 + \sin\Delta\phi$.

where the subscript indicates the path mode as in Fig 1.6. This interference is generalised by Hong-Ou-Mandel interference [24] for multiple photons. The biphoton state must then be represented by

a path entangled state:

$$|\psi\rangle = |2\rangle_1 |0\rangle_2 + e^{i2\theta} |0\rangle_1 |2\rangle_2 \tag{1.13}$$

In this case the oscillation of the detection probabilities depending on phase is twice as fast. $P_1 = 1 + \cos 2\Delta\phi$ and $P_2 = 1 + \sin 2\Delta\phi$.

This path encoded biphoton state is the same a two particle NOON state.

It is seen that the phase modulation increases linearly with the number of particles in the state $N\Delta\phi$. This would allow smaller phase changes to be detected faster by some quantum sensor, this is known as superresolution. It can also be seen that the error in the phase measurement becomes smaller for larger N. Consider the observable

$$O = |N, 0\rangle \langle 0, N| + |0, N\rangle \langle N, 0| \tag{1.14}$$

The error in the phase becomes

$$\Delta\phi = \frac{\Delta O}{|d \langle O\rangle / d\phi|} = \frac{1}{N} \tag{1.15}$$

Thus the phase error decreases with increasing particle number, this is known as supersensitivity.

NOON state super resolution can be achieved experimentally using quantum dots and an integrated photonic circuit [20], shown schematically here in Fig 1.7. The photons are generated sequentially from the QD, they are directed to a 50:50 beamsplitter where one is delayed. This causes 25% of the sequential photons to be time synched in parallel. QDs are resonantly excited in order to achieve long coherence times and good two photon interference visibilities. The two photons are then sent into a MZI, where they will interfere at the first DC, and generate a NOON state whereby detecting the coincidences. This NOON state then travels down paths 1 and 2. Gathering a phase because of the presence of the heater on path 1. from the outputs the phase of the MZI can be determined accurately.

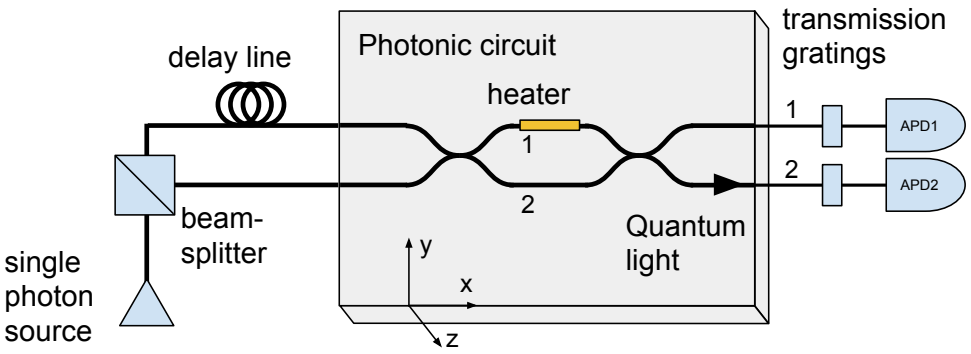

Figure 1.7: A single photon is emitted and impinges on the 50:50 beamsplitter, where one is delayed. The two photons will then interfere at the first DC, generating a NOON state. The state travels down paths 1 and 2, gathering a phase due to the presence of the heater on path 1. The phase of the MZI, and thus the temperature of the heater, can be determined accurately from analysing how output coincidences change with temperature.

In a photonic circuit, the phase of one arm is changed by inducing a refractive index change on that arm. This refractive index change causes a change in the phase of the circuit. This phase change is then measured with high resolution by the NOON state, allowing a superresolution measurement of whatever caused the refractive index change. Any component which changes the refractive index of one arm can then be sensed.

For example, in the circuit shown in Fig 1.7, placing a conducting gold strip over one arm will induce a refractive index change when there is a current run through the strip. This current can then be superresolved. If a microfluidic channel is placed in the path of the light going down one arm of the MZI, the fluid will have a different refractive index depending on its contents. This can be used to sense trace amounts of components inside the fluid [25].

In this example[20], the quantum light source and the photonic chip were not integrated. Meaning that experimentally this method is fragile and required a lot of manual alignment. If the QD source was bonded directly to the photonic circuit, and greater stability would be achieved, and also the potential to use this technique in real applications, not just in a lab.

1.4 Conclusion

This chapter contains an introduction to the theory of both quantum dots and photonic circuits. It also lays out the motivation for combining these technologies.

The rest of this thesis discusses a hybrid method for combining a quantum source with a photonic circuit. Chapter 2 discusses the theoretical and experimental methods used in designing and fabricating the hybrid device. Chapter 3 outlines the achieved results, a first demonstration of QDs integrated with photonic circuits with an active manipulation element. Chapter 4 discusses promising paths for future work.

Chapter 2

Methods and fabrication.

This Chapter outlines the methods used to fabricate the photonic circuits and quantum light source. Once the components are fabricated and tested independently, they are bonded to form the Hybrid device.

2.1 Waveguide fabrication and characterisation

The SiON waveguide chip devices were fabricated by plasma enhanced chemical vapour deposition to produce a layer of SiO_2 undercladding and SiON core on a silicon substrate. Electron-beam lithography and reactive ion etching were used to define the SiON core profile before finally an SiO_2 overclad layer was defined. During the lithography process arbitrary waveguide shapes can be imparted onto the device. These can be S-bends, directional couplers and/or Mach Zehnder interferometers. Once the fabrication of the device was complete the chips were then characterised. In this project the index of the core was 1.55 and the cladding was 1.51, the waveguide size was 1.6um to keep the guide single mode. This is done to ensure that two photon interference can occur inside the directional couplers.

Two V-groove arrays each were mounted on 6 axis stages which allowed precise alignment of the V-grooves to the side of the SiON waveguide chip. The V-grooves are commercially available arrays

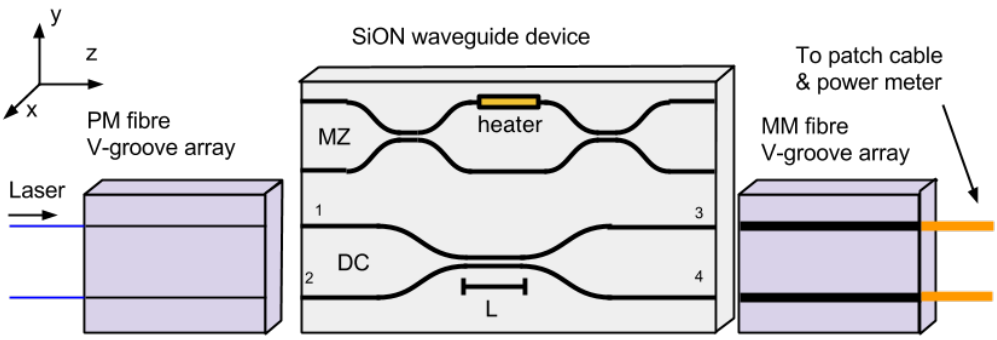

Figure 2.1: Schematic of waveguide characterisation experiment. Two PM V-groove arrays are aligned to the side of the waveguide chip. One of the V-groove channels injects laser light into port 1. The light is split by the DC and then collected from port 3 and 4 by another (generally multimode) V-groove array and sent to a power meter. The power ratios of of port 3 and 4 are used to calculate the coupling ratio of the DC.

of fibres. A substrate is patterned with an array of V shaped grooves into which optical fibres are planted and sealed, the polarisation axis of the polarisation maintaining (PM) fibre is aligned to the vertical axis of the chip. This experiment layout is shown in Figure 2.1. One of the PM fibres injects laser light into port 1. The laser used was a tuneable Fabry Perot cavity laser emitting in the range 890 to 935nm. This light propagates through the chip and is collected by the multimode V-groove array at ports 3 and 4 and is then sent to power meters. This allows the calculation of the coupling ratio of the directional couplers [26].

2.1.1 Directional coupler ratio measurement

Injecting light into port 1 and then 2 allows calculation of the coupling ratio which is independent of the coupling loss. The coupling ratio in the lossless case is as follows:

$$r = \frac{P_{13}}{I} = \frac{P_{24}}{I} \tag{2.1}$$

Where P_{ij} is the power measured at port j when light is injected into port i. The parameter I is the injected laser power. The conservation of power in the lossless case allows:

$$I = P_{13} + P_{14} = P_{23} + P_{24} \tag{2.2}$$

and

$$P_{13} + P_{24} = Ir \tag{2.3}$$

$$P_{14} + P_{23} = I(1 - r) \tag{2.4}$$

However since there exists coupling loss and at each port, given by l_i, the powers measured at each port become

$$P_{ij}^{'} = l_i l_j P_{ij} \tag{2.5}$$

Then by taking a power ratio the losses can be canceled

$$\frac{P_{13}^{'} P_{24}^{'}}{P_{14}^{'} P_{23}^{'}} = \frac{l_1 l_3 P_{13} l_2 l_4 P_{24}}{l_1 l_4 P_{14} l_2 l_3 P_{23}} \tag{2.6}$$

From Equation 2.3 and 2.1.1 this gives an expression for the coupling ratio

$$\left(\frac{r}{1-r}\right) * 2 = \frac{P_{13}^{'} P_{24}^{'}}{P_{14}^{'} P_{23}^{'}} \tag{2.7}$$

Rearranging to give

$$r = \frac{\sqrt{\frac{P_{13}^{'} P_{24}^{'}}{P_{14}^{'} P_{23}^{'}}}}{1 + \sqrt{\frac{P_{13}^{'} P_{24}^{'}}{P_{14}^{'} P_{23}^{'}}}} \tag{2.8}$$

This allows an accurate calculation of the coupling ratio which is independent of any coupling or alignment losses.

2.1.2 Mach Zehnder interferometer visibility measurement

In order to characterise the MZIs a very similar experiment was performed except that the powers were recorded as a voltage was applied to the heater. Then the effecive coupling ratio vs heater voltage was recorded. This shows how well the MZI can switch light between the two ports, this is quantified by calculating the visibility.

$$V = 100\frac{r_{max} - r_{min}}{r_{max} + r_{min}} \tag{2.9}$$

This percentage shows the maximum switching capability of the MZI. A visibility of 100% means that all of the light can be coupled to one port, with no light in the other. A visibility of 80% means that, at best, the MZI will send only 80% of the light to one port and 20% to the other.

2.2 Quantum dot growth and characterisation

2.2.1 Molecular beam epitaxy growth

The QD source was grown by molecular beam epitaxy (MBE)[27]. MBE allows deposition of various semiconductor layers with atomic precision of the layer height.

MBE take place in an ultra-high vacuum chamber, with pressures as low as 10^{-8} Pa. A target wafer, in this case (110) oriented GaAs, is placed in the chamber. The target materials, such as gallium and arsenic are placed in separated crucibles, and heated until they begin to sublime. The gaseous material will condense when it hits the wafer. If multiple elements hit the wafer together they may react, for example a gallium arsenide layer may be deposited.

By growing these layers carefully in StranskiKrastanov mode InAs quantum dots can be embedded into one of the layers. This layer is known as the wetting layer, the size and composition of which dictate the QD properties[28]. Strain and chemical potential define a critical layer thickness after which the growth of the layer will nucleate into small semiconductor 'islands' [29], inside which

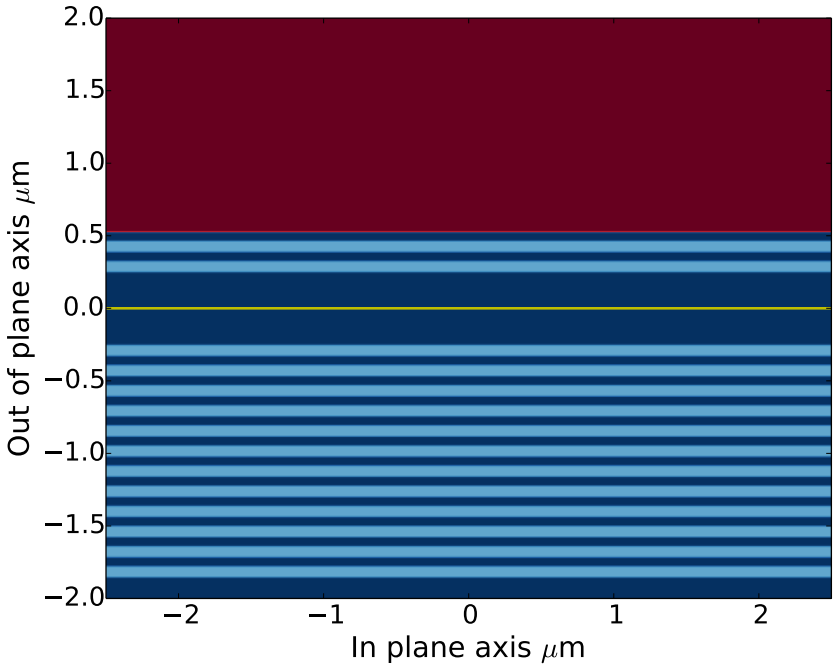

Figure 2.2: Index structure of the grown QD sample The red section is air with a refractive index of 1 and the alternating blue layers are GaAs and AlAs.

exist the QDs.

The QD sample used in this project were embedded in a planar distributed bragg reflector cavity to optimise the vertical emission mode from the QDs[30, 31, 32]. The index schematic of this structure is shown in Figure 2.2. The structure was grown on a GaAs substrate. Each reflector mirror repeat was made by a layer of GaAs and a layer of AlAs. The cavity was created by placing twelve mirror repeats of size $\lambda/4n$ where $\lambda = 910nm$ and n is the refractive index of the material. For GaAs this is 3.59 and for AlAs this is 2.97. Then a $2\lambda/n$ spacing of GaAs was grown with an embedded InAs layer 0.5nm thick. Finally two mirror repeats were grown on top. The emission wavelength is typically in the range 890 to 950nm.

2.2.2 Optical characterisation of quantum dots.

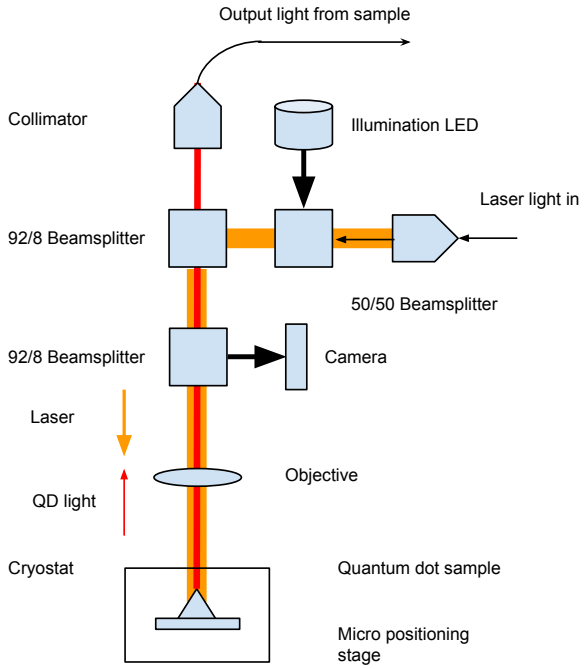

Figure 2.3: Typical micro-Photoluminescence setup to excite the QD sample with a laser and collect the QD light. The orange light is the laser and the red light is the path the QD light takes. The QD light travels in free space through two 92/8 beamsplitters, with 92% transmission. With the two beamsplitters; the laser, LED and CCD elements can be placed in the optical path of the QD light, while minimising the amount of QD light lost. The QD light is collected by a fibre coupled collimator and sent to a spectrometer equipped with a, liquid nitrogen cooled, silicon charged coupled device.

To characterise a QD source it is first placed in a cryostat and measured in the typical micro-Photoluminescence setup, shown in Figure 2.3. The setup was mounted on a 3-axis micrometer resolution stage in order to check different areas of the sample under test.

The source is mounted in a continuous Helium flow cryostat. The sample is kept below 10K for the duration of the experiments.

An LED is used to illuminate the sample, and a CCD camera allows realtime imaging of the position of the sample. The LED is red and is turned off during experiments so as not to excite the sample.

Above band laser excitation is used to excite the states in the sample. The fibre-coupled laser light is collimated and then sent in free space to the sample, through an infinity corrected objective lens. The objective normally offers 50x or 100x magnification.

The light from the sample is then sent in free space through two 92/8 beamsplitters, with 92% transmission. This is done so that the laser, LED and CCD elements can be placed in the optical path of the sample light, but that the minimum amount of sample light is lost.

The sample light is fibre coupled via collimator and sent to a silicon charged coupled device (liquid nitrogen cooled) equipped spectrometer.

2.2.3 Hanbury-Brown and Twiss measurements

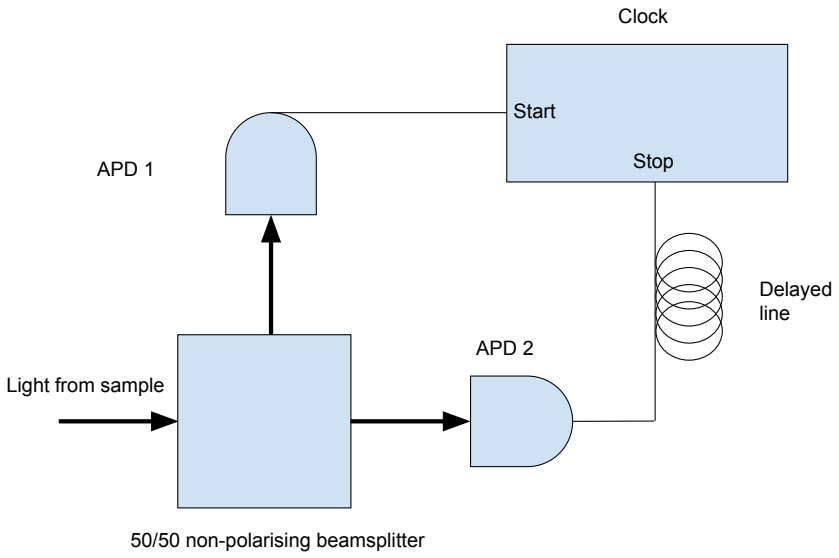

Figure 2.4: Typical HBT experiment, a stream of photons is sent to a balanced non-polarising beamsplitter. The split beam is then sent to two APDs whose signals are timestamped and correlated by a clock. The stop APD has a delay line in order to achieve negative correlation values.

To verify the single photon nature of the QD emission a Hanbury Brown and Twiss experiment must be performed[14]. The second order correlation function $g^{(2)}(\tau)$, as explained in Chapter 1, is measured by splitting a stream of photons by a DC or beamsplitter. This experiment is shown

schematically in Figure 2.4. Both streams are then sent to avalanche photodiodes (APDs) where the arrival time of each photon is measured. One APD starts a clock and the other stops it. By correlating the detection times of both APDs a correlation histogram is built up. One APD is delayed by some time τ in order to measure negative correlation values. An absence of counts at time $\tau = 0$ implies single photon emission.

2.3 Hybrid device

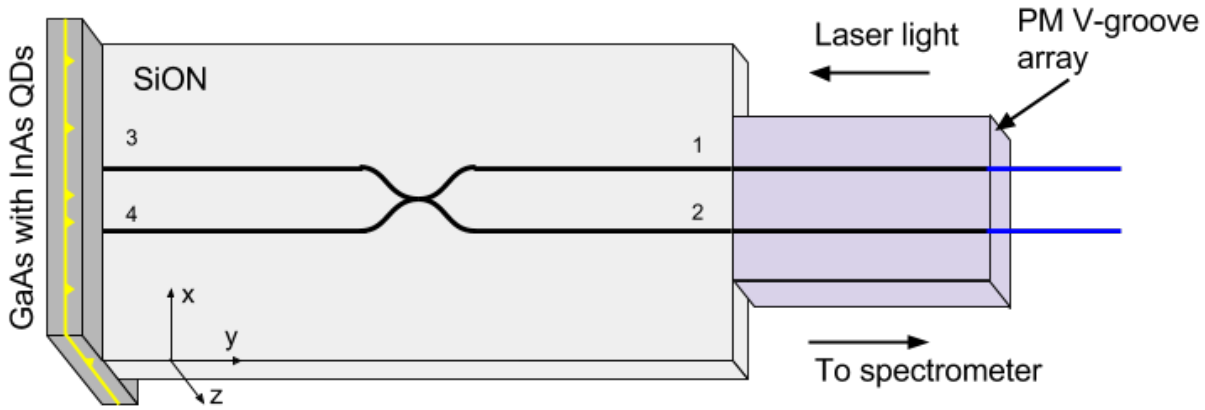

Figure 2.5: Schematic of a hybrid device. A III-V chip with embedded quantum dots is bonded to an SiON waveguide chip such that the single photons from the QDs are routed through the waveguides. The other end of the waveguide is bonded to a V-groove array to collect the light and send it to a spectrometer.

The III-V chip was bonded orthogonally to the SiON waveguide chip as shown in Figure 2.5 by UV cured adhesive. This allows the surface emission of the III-V chip to be collected by the waveguides. The DC is needed to allow separate fibres to be used for laser delivery and for QD light collection. The laser light is delivered through port 1. The laser power is split by the DC and will excite QDs at the ends of ports 3 and 4. This QD is collected by the waveguides and will be split by the DC and sent to ports 1 and 2. That which reaches port 2 is sent to the spectrometer. Typically the first experiment performed on a new device is to check the spectrum and to try and isolate a single QD, exhibited by a narrow well defined peak. Throughout this project the laser used was above the bandgap of GaAs, resonant or quasi-resonant excitation was not used. The device shown in

Figure 2.5 is useful only to check the emission of the QD into the waveguide, no on-chip quantum operations can take place because all the available waveguides are used for excitation and collection. In the next chapter a more sophisticated device with an on-chip MZI will be discussed.

2.3.1 Characterisation of quantum dots in hybrid circuit.

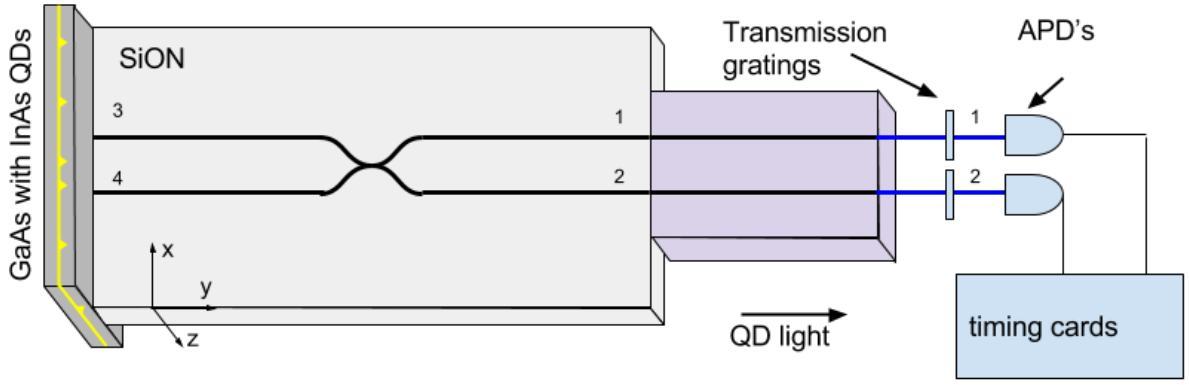

Figure 2.6: Schematic of HBT experiment taking place on the Hybrid chip. The light from ports 1 and 2 of the hybrid chip is collected by the V-groove array and sent towards transmission gratings in order to spectrally isolate the QD light. The light in both channels then impinge on APDs. The APD clicks are then correlated on a timing card.

In the case of the integrated hybrid chip, the HBT experiment, schematically shown in Figure 2.6, the beamsplitting takes plane using the directional coupler on-chip. But instead of sending the QD light from ports 1 and 2 to a spectrometer it is sent towards two monochromators. This is so that only the light from the target QD can be send towards the APDs and not background light, or light from other QDs.

Doing the experiment on-chip offers greater long term stability than a typical non-integrated QD experiment. In typical non-integrated HBT elaborate stability feedback loops need to implemented in order to keep the QD APD counts constant long enough to get a statistically significant result.

Chapter 3

Results

Various approaches for embedding QDs into integrated circuits are being explored. Photonic crystal waveguides yield high coupling efficiency of the QD emission into the in-plane propagating waveguide mode [33]. They have also demonstrated in-plane indistinguishable photons [34]. QDs integrated with ridge waveguides in GaAs have been reported integrated with on-chip superconducting single photon detectors [35]. Air clad GaAs ridge waveguides have also demonstrated QD integrated directional couplers [36, 37]. Other approaches use heralded single photons from spontaneous parametric down conversion integrated with waveguide chips [38] however this approach lacks the deterministic emission of quantum dots.

In this chapter, a platform for hybrid integration of III-V QDs with silicon oxynitride waveguides is presented. A GaAs chip containing InAs quantum dots are bonded orthogonally to the SiON chip such that the photons emitted from the surface of the GaAs chip are routed into a guided mode. The quantum dots are embedded in a low quality factor distributed Bragg reflector cavity with alternating layers of AlAs and GaAs. The SiON chip consists of a waveguide to deliver laser excitation light to the quantum dots and a return line through a Mach Zehnder interferometer. The orthogonal bonding method allows the surface emission from the QD to be collected by the waveguide. This orthogonal bonding is a major advantage of this hybrid integration method. The surface emission from the QD can be easily optimised by growing a distributed Bragg reflector cavity and/or creating a micropillar structure. Previous reports show efficiencies of out of plane

QD collection as high as 0.75 into free space high numerical aperture objectives [39, 40]. In the device presented here, the SiON waveguide numerical aperture is 0.3. The hybrid platform also has the potential for diode structures to be created for electrically driven or tuneable QD devices integrated with the waveguides.

In this chapter, first theoretical simulations of the device are discussed. These calculations were used to deduce the theoretical efficiency of the device and to optimise parameters. Then the development of high-quality waveguides circuits is presented. Followed by a discussion of the created hybrid device. Sections of this chapter, specifically the Hybrid integrated devices section, are as a result of work which has been recently published [41].

3.1 Simulations and design

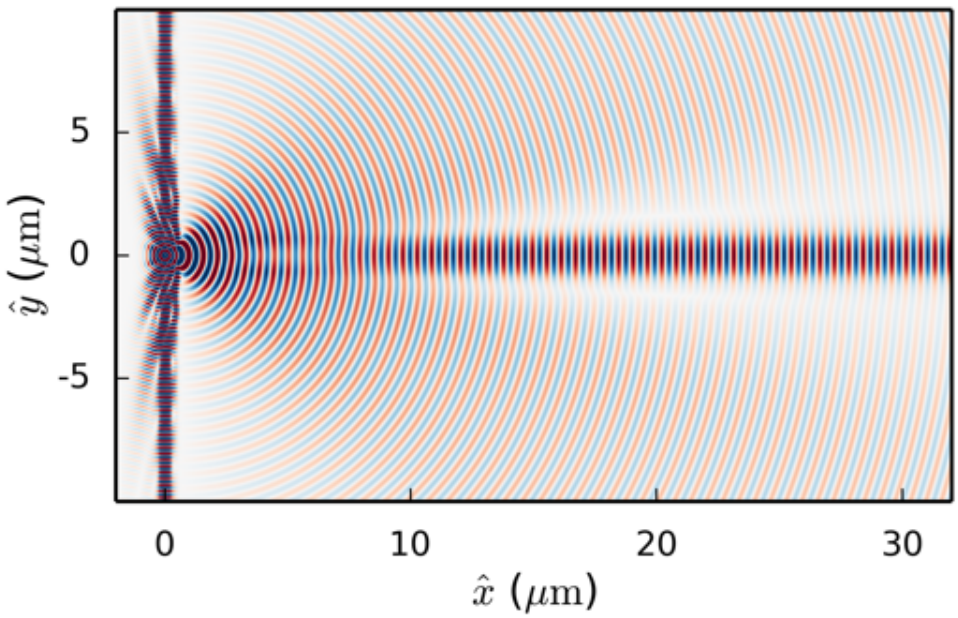

Figure 3.1: Finite difference time domain simulation of a QD dipole emitting in a cavity and the emission being guided by the SiON core. The $\hat{z}$ component of the electro-magnetic field is clearly seen to propagate along the waveguide core.

The characteristics of the device were simulated by using the finite difference time domain package

MEEP [42, 43]. A $\hat{z}$ oriented dipole emitter was placed in the centre of the cavity spacer aligned to the centre of the waveguide. A perfectly matched layer was placed at the edges of the simulation domain to absorb all light and prevent unwanted reflections. The $\hat{z}$ component of the electric field is shown in Figure 3.1. There is a clear emission pattern along the waveguide core. The efficiency of this device was also determined theoretically. A bounding box which records the Fourier transformed fields was placed at the edge of the domain and just inside the perfectly matched layer.

From this bounding box the total power spectrum is recorded when the system is excited with a short Gaussian pulse. Another flux plane is placed across the waveguide. The waveguide core size was 1.6 μm, in order to keep te guides single mode, and the far field propagating mode has a spatial $1/e$ width of 1.88 μm which was chosen as the size of the waveguide flux plane. It is placed sufficiently far from the surface of the III-V cavity enhanced-chip so that only the waveguide propagating mode is measured. Taking the ratio of the light propagating in the waveguide to the total in the bounding box gives the efficiency of the hybrid collection system. At the centre of the cavity wavelength the efficiency is 2.8%. For a QD emitting into free space with no cavity a collection of 0.5% can be expected into a 0.5 NA objective. When the QD is in a cavity the efficiency can rise to 7% depending on the number of mirror repeats and the numerical aperture of the collection objective. For the device presented here the numerical aperture of the waveguide is 0.35 and the III-V sample has a planar cavity with Bragg 12 repeats below the QD layer and 2 repeats above. This efficiency of 2.8% is almost exactly in line with what has previously been estimated for free space collection with the same NA and same number of repeats [44].

3.2 Waveguide devices

As explained in the Chapter 2, by placing two waveguides in close proximity the light can couple between them. The power in each waveguide at a position L is given by

$$P_1(L) = I\cos^2 cL \tag{3.1}$$

$$P_2(L) = I\sin^2 cL \tag{3.2}$$

where I is the input laser intensity, c is the coupling coefficient related to the waveguide index contrast, the separation between the guides and the wavelength. These equations allow the design of DCs with a well defined coupling ratio by changing the interaction length L. To test this a set of chips were fabricated with DCs of increasing interaction length L and the coupling ratio was measured for each. The results are shown in Figure 3.2. The differing black and red squares and circles are simply different chips from the same wafer. The red line is a $\sin^2$ fit to the data. The results show good consistency between chips, and the behaviour matches the expected sinusoid. This allows the creation of devices with embedded DCs with any coupling ratio, defined by the fabrication process. For example, to do on-chip Hanbury Brown and Twiss a DC with $r = 1/2$ is needed. For a photonic quantum CNOT gate a series of DCs with ratios $r = 1/2$ and $r = 1/3$ is needed.

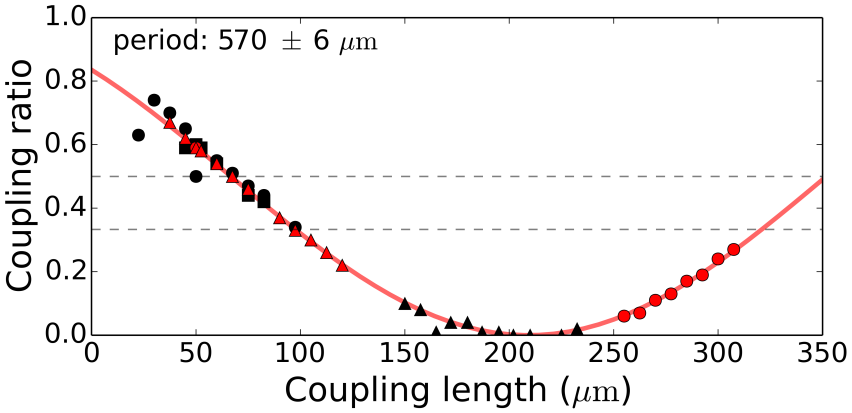

Figure 3.2: Measured coupling ratio vs interaction length for a set of waveguide chips. The results show the expected smooth sinusoidal behaviour.

Another important parameter for a waveguide device is its operating wavelength, depending on the III-V source used, the waveguide device would need to operate in the range 900-950nm for the current QD devices, however the QDs can achieve telecom wavelengths. The properties of a DC will change depending on the wavelength of the light. To check this, one DC was analysed by varying laser wavelength and monitoring the coupling ratio, this result is shown in Figure 3.3.

As is seen in Figure 3.3 , there is a linear decrease in the coupling ratio with increasing wavelength for the measured chip. In general the wavelength dependence is always linear, however whether the slope is positive or negative depends on other chip parameters, such as length, period of the length

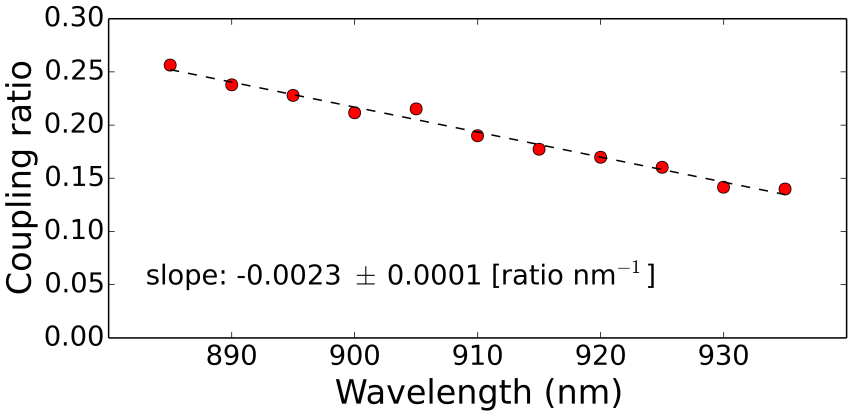

Figure 3.3: Measured DC coupling ratio vs laser wavelength for a device. The red line is a linear fit to the data.

dependence and index contrast.

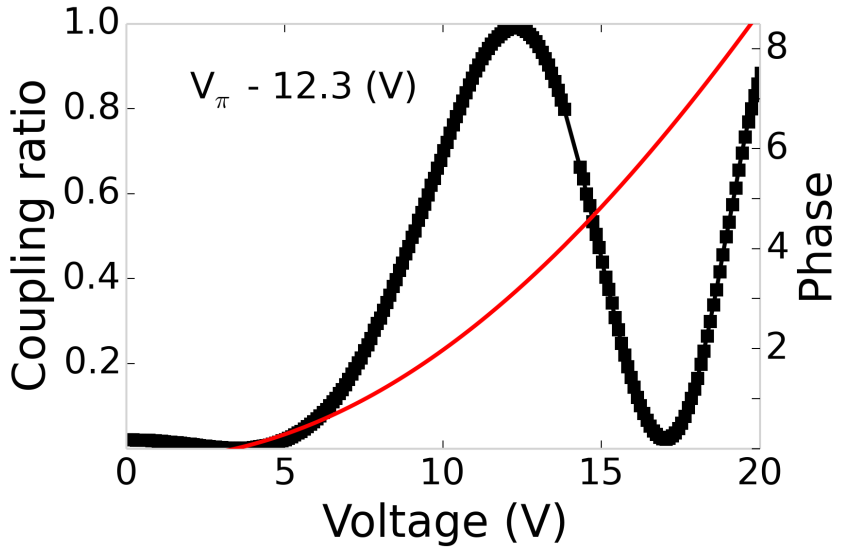

Figure 3.4: Performance of an SiON based Mach Zehnder interferometer. The black line traces the coupling ratio vs applied voltage and the red line is the phase calculated from the data.

Mach Zehnder interferometers are very interesting devices for their applications in quantum computing, by way of a qubit preparation device, and in telecommunications, as a light modulator. The MZIs were fabricated as described in Chapter 2 by placing two DCs in series with a phase changing element on one arm, in this case a heater causes a refractive index change which induces

a phase change. The coupling ratio was monitored as the heater voltage was varied. The result is shown in Figure 3.4. The black squares are the coupling ratio as the voltage was varied and the red line is the calculated phase. The phase was calculated using a pre-established model [26]. The visibility of this MZI was 99.7 $\pm$ 0.06 %. To apply a π phase shift to the light in one arm in this case would need 12.3 V applied to the heater.

In this section the development of high quality photonic circuits was described. Performing quantum operations on chip offers greater stability and scalability than can be done with bulk optics. In the next section the photonic circuits will be combined with the QD source in order to make an integrated platform capable of operating on the quantum light emitted by the QDs.

3.3 Hybrid integrated devices

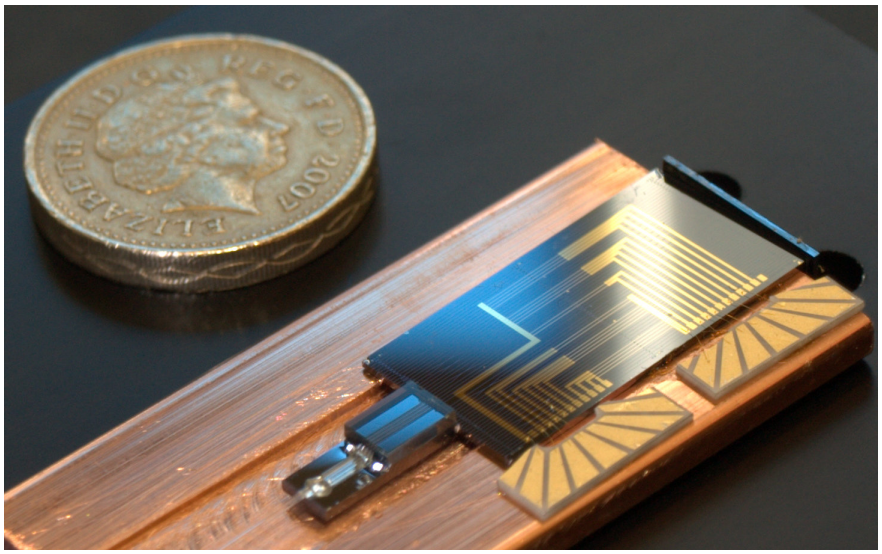

Figure 3.5: Photograph of an example bonded device. The III-V chip is bonded orthogonally to the SiON chip (top-right) which is in turn bonded to a six channel V-groove array (bottom-left of chip). The nichrome channels allow a phase-varying heating current to be applied to the MZ's. The structure is glued to a copper block is placed in a cryostat for the duration of experiments.

Figure 3.5 shows a photograph of an example device. A strip of microcavity wafer containing QDs is bonded to one end of the SiON waveguide chip. In SiON the waveguide numerical aperture

is limited by $\sqrt{n_{core}^2 - n_{clad}^2}$, where $n_{core} = 1.55$ and $n_{clad} = 1.51$. The photons are routed into the waveguides, two sequential directional couplers form a MZI with a nichrome heater applying a local phase shift to one MZI arm. This SiON technology is compatible with the creation of arbitrary designs of beamsplitters, MZIs and phase shifters. As explained in the previous chapter, a polarisation maintaining fibre array is aligned and attached to the waveguides for collection of photons and the device is cooled to 4K for the duration of the experiment.

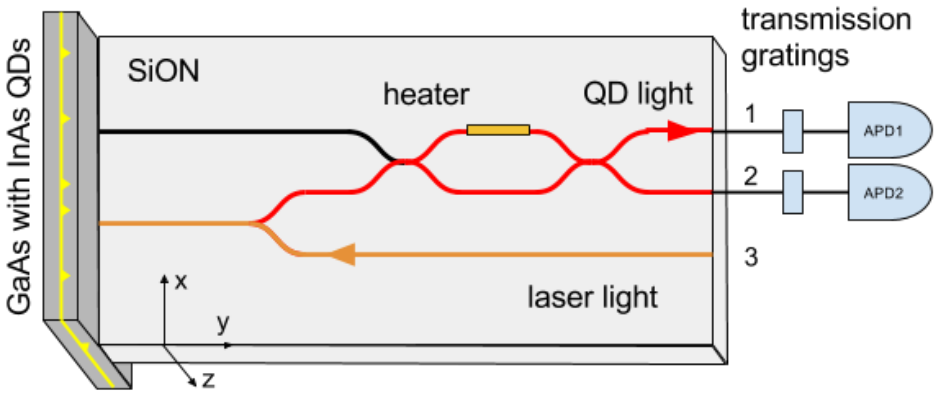

Figure 3.6: Schematic of the experiment. The laser light travels from port 3 (highlighted in orange) exciting QDs in the III-V chip. The QD light (path highlighted in red) enters a heater tuned MZI. The QD light is collected by V-grooves and sent through transmission gratings towards APDs in order to do correlations.

Figure 3.6 shows the optical schematic of the experiments. A single channel delivers laser light. The QD light is returned through the MZI and collected into the fibre array. The fibres are sent directly to a spectrometer. For time resolved experiments transmission gratings are used to spectrally filter the emission before sending the light to avalanche photodiodes.

The integrated device is fixed and there is no freedom to analyse different QDs on the III-V sample once the bonding is complete. This creates stability and no drifting in emission intensity is seen over the course of 12 hours. The QD intensity as a function of time is plotted in Figure 3.9. A reasonably high density QD sample is used to ensure that a dot which is emits in the centre cavity mode is aligned with a waveguide. The central cavity wavelength is at 910nm. The spectrum from both outputs of the device can be seen in Figure 3.7. The MZI was tuned to 50:50, and it is seen that the spectrum from both output arms is identical. The QD analysed was the one at the centre

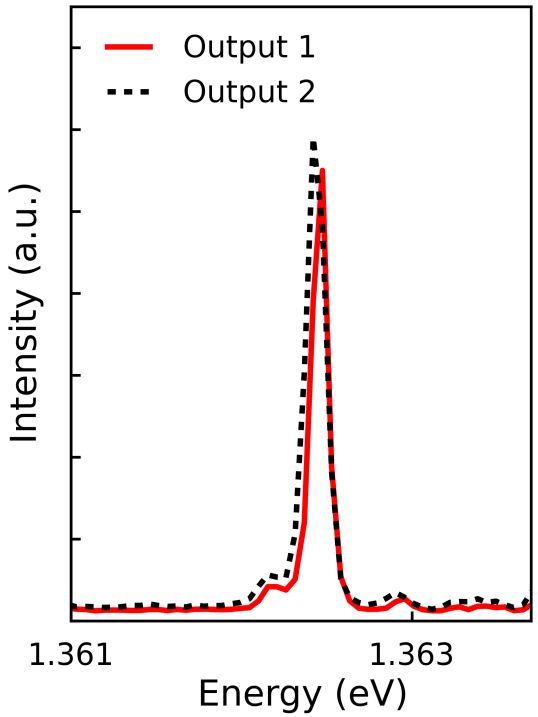

Figure 3.7: Spectrum of a quantum dot from both output ports of the device indicated in black and red.

of the cavity mode at 1.362 eV.

A power dependence was recorded, seen in Figure 3.8. The emission, before saturation, is approximately linear ($P^{0.95}$) implying an exciton and not a higher order complex [45]. The peak exhibits no fine structure splitting typically seen in a neutral exciton [46, 47] so it is likely charged.

To verify the single photon nature of the QD emission, a Hanbury Brown and Twiss experiment was recorded using the on-chip MZI as a beamsplitter. The emission from both arms was sent through two different transmission gratings for spectral filtering and then sent to avalanche photodiodes. The signal in one arm was delayed so as to measure negative correlation times. An absence of correlation coincidences at time $\tau = 0$ implies single photon emission. The second order correlation curves were taken under continuous wave (λ = 810nm) and pulsed (λ = 850nm) excitation. The curves are shown in Figure 3.10. In the case of the pulsed curve (shown in Figure 3.10 (a)) the signal to noise ratio due to dark counts, ($\sim$ 100 vs $\sim$ 1500 QD counts), of the detectors was calculated and the resulting dark count contribution was subtracted. A time window was also applied to the

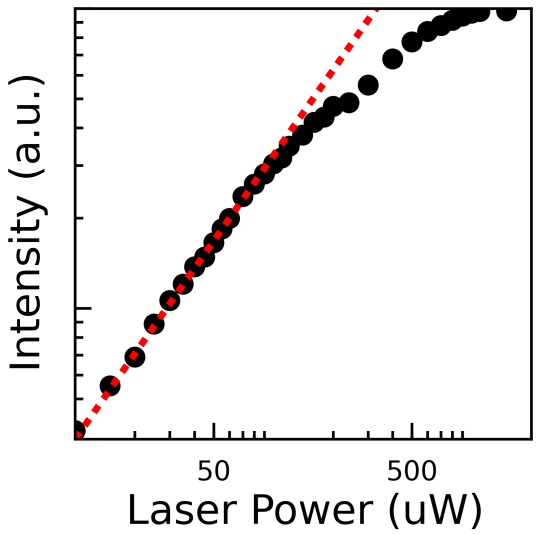

Figure 3.8: Recorded dependence of the QD emission intensity on the laser power, the solid line is a fit to the data. There is a linear dependance between QD intensity and laser power implying the transition is from an exciton state.

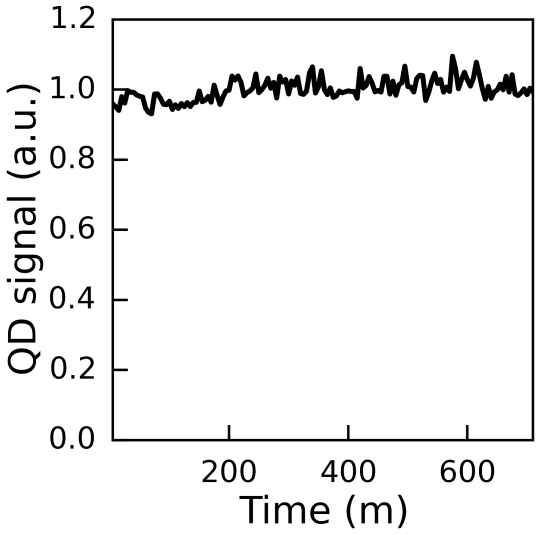

Figure 3.9: Counts measured as a function of time over 12 hours. The hybrid chip is stable over long periods of time and needs no drifting correction.

data. Since the lifetime of the QD was 670 ± 3ps, the vast majority (96%) of QD emission resides in a 4ns window. So only coincidences inside this window were used for calculating the $g^{(2)}(0)$ value

of 0.19.

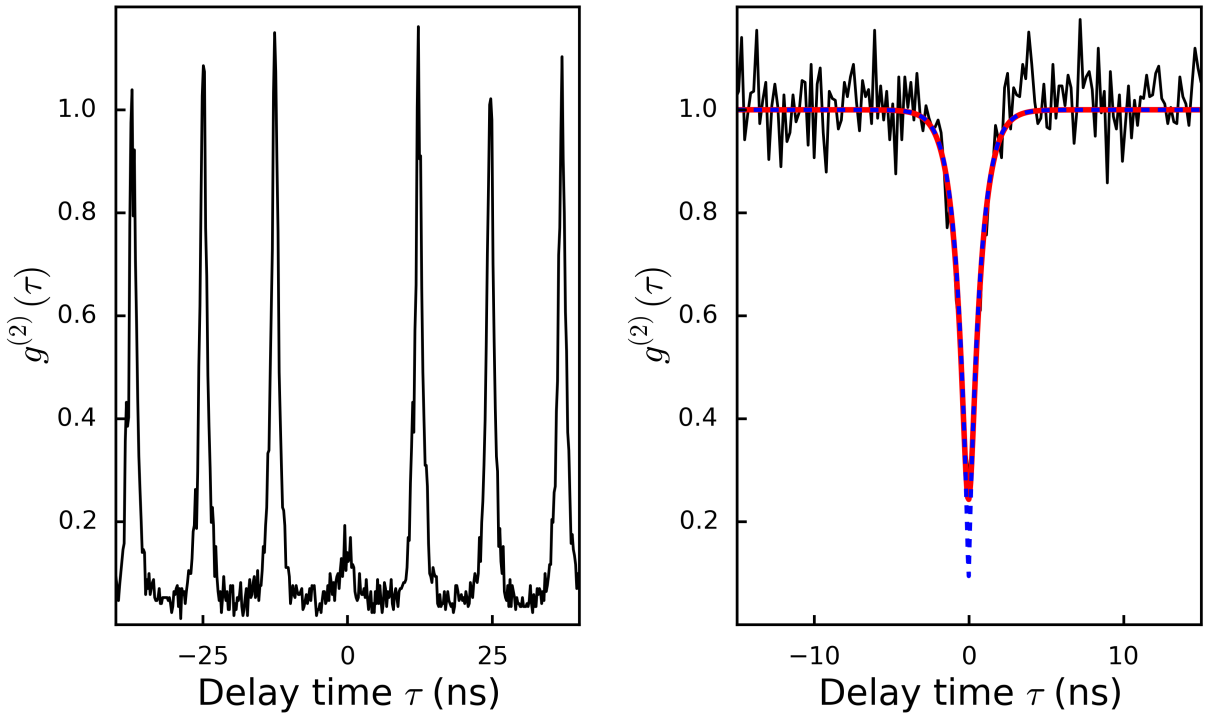

Figure 3.10: (a) Second order correlation function under pulsed excitation (b) Second order correlation function under continuous wave excitation. The black line is the raw data, the red line is a fit taking the system response function into account, and the dashed blue line is the fit deconvoluted with the response function.

In the CW case as seen in Figure 3.10 (b) the black line corresponds to the data, the red solid line corresponds to a fit and the blue line to a deconvoluted fit. The deconvolution was done to subtract the response function of the detectors and timing system. The $g^{(2)}(0)$ was taken from the deconvoluted to be 0.09.

The active modulation of the MZI was tested on the single photon source. A voltage was applied to the heater on one arm of the MZI which induces local heating of the arm and a change in the refractive index of the waveguide core. This creates a relative phase between the light in each arm. The emission coupling to each output arm of the MZI then varies as a function of the applied voltage. This coupling, along with calculated phase, is shown in Figure 3.11.

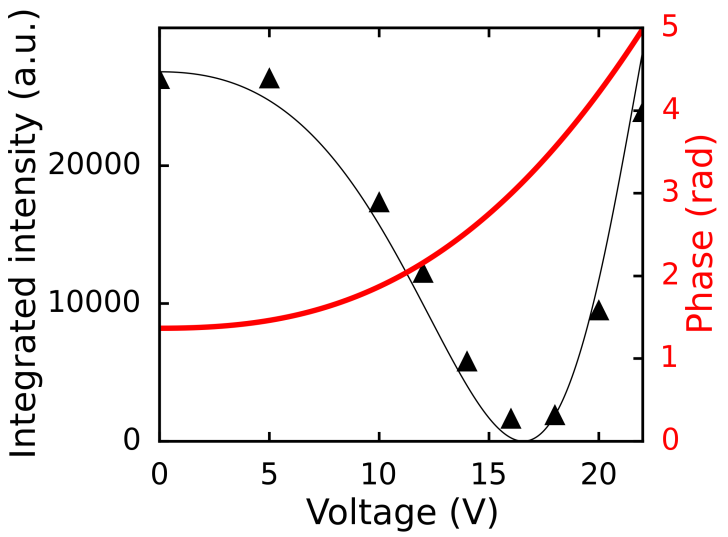

Figure 3.11: The output of a MZI arm is shown by the black triangles, the solid black line is a fit to the data. The red line is the calculated phase as a function of voltage.

The model was based on calculating the expected power output of each port as a function of coupling ratio and phase. The expected power is based on the matrix model of a phase shift operation between two directional couplers [48]. The model of the phase the same as the one used in Section 3.2[26].

In conclusion a novel method for integrating a III-V quantum light source with an SiON waveguide platform has been demonstrated. The single photon nature of the source was verified using on-chip components and the active modulation of the emission was demonstrated. This device shows potential for integration of site controlled [7] QDs granting precise alignment of multiple QDs with multiple waveguides allowing for scalable quantum manipulation.

Chapter 4

Future work

This document outlines work undertaken to design and fabricate an integrated device which emits and modulates single photon emission. This device has great potential in the field of quantum information science however some challenges still need to be over come.

The device efficiency was calculated to be 2.8%. This needs to improve to make a practical device. The orthogonal bonding technique of the hybrid device however has the advantage that the surface emission from a III-V chip is easily optimised. The planar cavity used so far in this project emits most of the light into the plane of the cavity and not to the surface of the device. This can be negated by creating some kind of micropillar or nanowire device where the mode directs all of the emission to the surface. The challenges with this approach would be how to align the micropillars with the waveguides. Another approach would be to change the index contrast of the waveguides. Currently the cladding index of 1.51 and the SiON core index is 1.55, this core index can be changed by varying the nitrogen concentration and could allow core indices upto 2. This would increase the NA of the waveguide and collect more of the light emitted from the surface of the III-V. A better mode matching between the waveguides and optical fibres could be achieved by tapering the ends of the waveguides and/or by using fibres with a lensed ends which alter the output mode size.

Other important aspect of the device which need to be addressed is the alignment of the III-V source. For a device which performs real operations many QD photons need to interact on the

chip. Many QDs need to be aligned with many waveguides. This could be done using positioned QDs.

In order to make many photons interfere on-chip the QDs need to be wavelengths tunable. This could be achieved using QDs embedded in an electrically controlled diode. This would allow the application of an electric field to the QD to change the band structure and the emission energy of the photons. This would allow many photons at the same wavelength propagate through the chip where real logic operations could take place.

Bibliography

[1] Emanuel Knill, Raymond Laflamme, and Gerald J Milburn. A scheme for efficient quantum computation with linear optics. *Nature*, 409(6816):46–52, 2001.

[2] Jeremy L O'Brien, Geoffrey J Pryde, Andrew G White, Timothy C Ralph, and David Branning. Demonstration of an all-optical quantum controlled-not gate. *Nature*, 426(6964):264–267, 2003.

[3] Jacques Carolan, Chris Harrold, Chris Sparrow, Enrique Martín-López, Nicholas J Russell, Joshua W Silverstone, Peter J Shadbolt, Nobuyuki Matsuda, Manabu Oguma, Mikitaka Itoh, et al. Universal linear optics. *arXiv preprint arXiv:1505.01182*, 2015.

[4] A. J. Bennett, D. C. Unitt, P. Atkinson, D. A. Ritchie, and A. J. Shields. High performance single photon sources from photolithographically defined pillar microcavities. *Opt. Express*, 13(1):50–55, Jan 2005.

[5] Yu-Ming He, Yu He, Yu-Jia Wei, Dian Wu, Mete Atatüre, Christian Schneider, Sven Höfling, Martin Kamp, Chao-Yang Lu, and Jian-Wei Pan. On-demand semiconductor single-photon source with near-unity indistinguishability. *Nature nanotechnology*, 8(3):213–217, 2013.

[6] RM Stevenson, CL Salter, J Nilsson, AJ Bennett, MB Ward, I Farrer, DA Ritchie, and AJ Shields. Indistinguishable entangled photons generated by a light-emitting diode. *Physical review letters*, 108(4):040503, 2012.

[7] Gediminas Juska, Valeria Dimastrodonato, Lorenzo O Mereni, Agnieszka Gocalinska, and Emanuele Pelucchi. Towards quantum-dot arrays of entangled photon emitters. *Nature Photonics*, 7(7):527–531, 2013.

[8] Alberto Politi, Jonathan CF Matthews, Mark G Thompson, and Jeremy L O'Brien. Integrated quantum photonics. *Selected Topics in Quantum Electronics, IEEE Journal of*, 15(6):1673–1684, 2009.

[9] Jianwei Wang, Alberto Santamato, Pisu Jiang, Damien Bonneau, Erman Engin, Joshua W Silverstone, Matthias Lermer, Johannes Beetz, Martin Kamp, Sven Höfling, et al. Gallium arsenide (gaas) quantum photonic waveguide circuits. *Optics Communications*, 327:49–55, 2014.

[10] Yanfeng Zhang, Loyd McKnight, Erman Engin, Ian M. Watson, Martin J. Cryan, Erdan Gu, Mark G. Thompson, Stephane Calvez, Jeremy L. OBrien, and Martin D. Dawson. Gan directional couplers for integrated quantum photonics. *Applied Physics Letters*, 99(16):–, 2011.

[11] Alberto Politi, Martin J Cryan, John G Rarity, Siyuan Yu, and Jeremy L O'Brien. Silica-on-silicon waveguide quantum circuits. *Science*, 320(5876):646–649, 2008.

[12] Thomas Gerrits, Nicholas Thomas-Peter, James C Gates, Adriana E Lita, Benjamin J Metcalf, Brice Calkins, Nathan A Tomlin, Anna E Fox, Antía Lamas Linares, Justin B Spring, et al. On-chip, photon-number-resolving, telecommunication-band detectors for scalable photonic information processing. *Physical Review A*, 84(6):060301, 2011.

[13] Robert H Hadfield. Single-photon detectors for optical quantum information applications. *Nature photonics*, 3(12):696–705, 2009.

[14] R Hanbury Brown and RQ Twiss. A test of a new type of stellar interferometer on sirius. *Nature*, 178(4541):1046–1048, 1956.

[15] Bahaa EA Saleh and Malvin Carl Teich. *Fundamentals of photonics*, volume 22. Wiley New York, 1991.

[16] MA Pooley, DJP Ellis, RB Patel, AJ Bennett, KHA Chan, I Farrer, DA Ritchie, and AJ Shields. Controlled-not gate operating with single photons. *Applied Physics Letters*, 100(21):211103, 2012.

[17] C Varnava, RM Stevenson, J Nilsson, J Skiba-Szymanska, B Dzurňák, M Lucamarini, RV Penty, I Farrer, DA Ritchie, and AJ Shields. An entangled-led driven quantum relay over 1 km. *arXiv preprint arXiv:1506.00518*, 2015.

[18] Sacha Kocsis, Guo-Yong Xiang, Tim C Ralph, and Geoff J Pryde. Heralded noiseless amplification of a photon polarization qubit. *Nature Physics*, 9(1):23–28, 2013.

[19] A Zavatta, J Fiurášek, and M Bellini. A high-fidelity noiseless amplifier for quantum light states. *Nature Photonics*, 5(1):52–60, 2011.

[20] AJ Bennett, JP Lee, DJP Ellis, T Meany, E Murray, F Floether, JP Griffths, I Farrer, DA Ritchie, and AJ Shields. Cavity-enhanced coherent light scattering from a quantum dot. *arXiv preprint arXiv:1508.01637*, 2015.

[21] Itai Afek, Oron Ambar, and Yaron Silberberg. High-noon states by mixing quantum and classical light. *Science*, 328(5980):879–881, 2010.

[22] Vittorio Giovannetti, Seth Lloyd, and Lorenzo Maccone. Advances in quantum metrology. *Nature Photonics*, 5(4):222–229, 2011.

[23] Jaewoo Joo, William J. Munro, and Timothy P. Spiller. Quantum metrology with entangled coherent states. *Phys. Rev. Lett.*, 107:083601, Aug 2011.

[24] CK Hong, ZY Ou, and Leonard Mandel. Measurement of subpicosecond time intervals between two photons by interference. *Physical Review Letters*, 59(18):2044, 1987.

[25] Andrea Crespi, Mirko Lobino, Jonathan CF Matthews, Alberto Politi, Chris R Neal, Roberta Ramponi, Roberto Osellame, and Jeremy L OBrien. Measuring protein concentration with entangled photons. *Applied Physics Letters*, 100(23):233704, 2012.

[26] Jonathan CF Matthews, Alberto Politi, André Stefanov, and Jeremy L O'Brien. Manipulation of multiphoton entanglement in waveguide quantum circuits. *Nature Photonics*, 3(6):346–350, 2009.

[27] AY Cho and JR Arthur. Molecular beam epitaxy. *Progress in solid state chemistry*, 10:157–191, 1975.

[28] Seungwon Lee, Olga L. Lazarenkova, Paul von Allmen, Fabiano Oyafuso, and Gerhard Klimeck. Effect of wetting layers on the strain and electronic structure of inas self-assembled quantum dots. *Phys. Rev. B*, 70:125307, Sep 2004.

[29] D. J. Eaglesham and M. Cerullo. Dislocation-free stranski-krastanow growth of ge on si(100). *Phys. Rev. Lett.*, 64:1943–1946, Apr 1990.

[30] AJ Bennett, DC Unitt, P See, AJ Shields, P Atkinson, K Cooper, and DA Ritchie. Microcavity single-photon-emitting diode. *Applied Physics Letters*, 86(18):1102, 2005.

[31] David J P Ellis, Anthony J Bennett, Samuel J Dewhurst, Christine A Nicoll, David A Ritchie, and Andrew J Shields. Cavity-enhanced radiative emission rate in a single-photon-emitting diode operating at 0.5?ghz. *New Journal of Physics*, 10(4):043035, 2008.

[32] A. J. Bennett, D. C. Unitt, A. J. Shields, P. Atkinson, and D. A. Ritchie. Influence of exciton dynamics on the interference of two photons from a microcavity single-photon source. *Opt. Express*, 13(20):7772–7778, Oct 2005.

[33] Andre Schwagmann, Sokratis Kalliakos, Ian Farrer, Jonathan P Griffiths, Geb AC Jones, David A Ritchie, and Andrew J Shields. On-chip single photon emission from an integrated semiconductor quantum dot into a photonic crystal waveguide. *Applied Physics Letters*, 99(26):261108, 2011.

[34] Sokratis Kalliakos, Yarden Brody, Andre Schwagmann, Anthony J Bennett, Martin B Ward, David JP Ellis, Joanna Skiba-Szymanska, Ian Farrer, Jonathan P Griffiths, Geb AC Jones, et al. In-plane emission of indistinguishable photons generated by an integrated quantum emitter. *Applied Physics Letters*, 104(22):221109, 2014.

[35] Günther Reithmaier, Stefan Lichtmannecker, Thorsten Reichert, Peter Hasch, Kai Müller, Max Bichler, Rudolf Gross, and Jonathan J Finley. On-chip time resolved detection of quantum dot emission using integrated superconducting single photon detectors. *Scientific reports*, 3, 2013.

[36] N Prtljaga, RJ Coles, J O'Hara, B Royall, E Clarke, AM Fox, and MS Skolnick. Monolithic integration of a quantum emitter with a compact on-chip beam-splitter. *Applied Physics Letters*, 104(23):231107, 2014.

[37] Klaus D Jöns, Ulrich Rengstl, Markus Oster, Fabian Hargart, Matthias Heldmaier, Samir Bounouar, Sven M Ulrich, Michael Jetter, and Peter Michler. Monolithic on-chip integration of semiconductor waveguides, beamsplitters and single-photon sources. *arXiv preprint arXiv:1403.7174*, 2014.

[38] Thomas Meany, Lutfi A Ngah, Matthew J Collins, Alex S Clark, Robert J Williams, Benjamin J Eggleton, MJ Steel, Michael J Withford, Olivier Alibart, and Sébastien Tanzilli.

Hybrid photonic circuit for multiplexed heralded single photons. *Laser & Photonics Reviews*, 8(3):L42–L46, 2014.

[39] Julien Claudon, Joël Bleuse, Nitin Singh Malik, Maela Bazin, Périne Jaffrennou, Niels Gregersen, Christophe Sauvan, Philippe Lalanne, and Jean-Michel Gérard. A highly efficient single-photon source based on a quantum dot in a photonic nanowire. *Nature Photonics*, 4(3):174–177, 2010.

[40] Mathieu Munsch, Nitin S Malik, Emmanuel Dupuy, Adrien Delga, Joël Bleuse, Jean-Michel Gérard, Julien Claudon, Niels Gregersen, and Jesper Mørk. Dielectric gaas antenna ensuring an efficient broadband coupling between an inas quantum dot and a gaussian optical beam. *Physical review letters*, 110(17):177402, 2013.

[41] E. Murray, D. J. P. Ellis, T. Meany, F. F. Floether, J. P. Lee, J. P. Griffiths, G. A. C. Jones, I. Farrer, D. A. Ritchie, A. J. Bennett, and A. J. Shields. Quantum photonics hybrid integration platform. *Applied Physics Letters*, 107(17), 2015.

[42] Ardavan F Oskooi, David Roundy, Mihai Ibanescu, Peter Bermel, John D Joannopoulos, and Steven G Johnson. Meep: A flexible free-software package for electromagnetic simulations by the fdtd method. *Computer Physics Communications*, 181(3):687–702, 2010.

[43] Vladimir A Mandelshtam and Howard S Taylor. Harmonic inversion of time signals and its applications. *The Journal of chemical physics*, 107(17):6756–6769, 1997.

[44] AJ Bennett, P Atkinson, P See, MB Ward, RM Stevenson, ZL Yuan, DC Unitt, DJP Ellis, K Cooper, DA Ritchie, et al. Single-photon-emitting diodes: a review. *physica status solidi (b)*, 243(14):3730–3740, 2006.

[45] M Grundmann and D Bimberg. Theory of random population for quantum dots. *Physical Review B*, 55(15):9740, 1997.

[46] M Bayer, G Ortner, O Stern, A Kuther, AA Gorbunov, A Forchel, Pawel Hawrylak, S Fafard, K Hinzer, TL Reinecke, et al. Fine structure of neutral and charged excitons in self-assembled in (ga) as/(al) gaas quantum dots. *Physical Review B*, 65(19):195315, 2002.

[47] D Gammon, ES Snow, BV Shanabrook, DS Katzer, and D Park. Fine structure splitting in the optical spectra of single gaas quantum dots. *Physical review letters*, 76(16):3005, 1996.

[48] R Clark Jones. A new calculus for the treatment of optical systems. *JOSA*, 31(7):488–493, 1941.